Advanced Materials

ADVANCED MATERIALS
www.advmat.de

RESEARCH ARTICLE

Tailored Arylboronic Acid Derivatives Stabilize Perovskite Octahedron in Inverted Perovskite Solar Cells

Min Wang | Jinhui Wang | Peng Cui | Xing Zhao | Liang Li | Junjie Zhou | Zeze Chen | Yi Suo | Yi Lu | Xin Sun | Meicheng Li

State Key Laboratory of Alternate Electrical Power System with Renewable Energy Sources, School of New Energy, North China Electric Power University, Beijing, China

Correspondence: Liang Li (lili514091@ncepu.edu.cn) | Meicheng Li (mcli@ncepu.edu.cn)

Received: 6 December 2025 | **Revised:** 30 January 2026 | **Accepted:** 6 February 2026

Keywords: buried interface | coplanar multidentate anchoring | perovskite octahedron | perovskite solar cells

ABSTRACT

The absence of halide ions in perovskite at the buried interface remains a critical factor restricting the stability in efficient inverted perovskite solar cells (PSCs), mainly due to the metastable perovskite lattice. Herein, through a systematic investigation of the bonding mechanisms between arylboronic acid derivatives and perovskite, designing 5-fluoro-6-hydroxypyridin-3-ylboronic acid (FO-PyBA) anchors robustly on the perovskite surface vacancies to reinforce the perovskite octahedron to stabilize the buried interface. The $-B(OH)_2$ and C═O groups in FO-PyBA promote the concurrent formation of C═O—Pb and B—O—Pb coordination bonds alongside N—H···I and O—H···I hydrogen bonds, which establish a robust coplanar multidentate anchoring with perovskite to reinforce the octahedral framework. Crucially, this more stable multidentate anchoring is enabled by precisely tailoring the interatomic distances of anchoring sites in derivatives to match the defect sites of perovskite. The FO-PyBA effectively suppresses Pb/I vacancy defects and iodine ions migration to reduce interfacial nonradiative recombination. Consequently, it enabled inverted PSCs achieving a champion efficiency of 26.85% (certificated 26.70%) and maintained 94% of its initial efficiencies after 1000 h of operating under one-sun illumination in N_2.

1 | Introduction

Inverted perovskite solar cells (PSCs) exhibit significant commercialization potential, particularly due to their high compatibility with flexible and multi-junction solar cell technology [1–3]. Owing to the advancements in self-assembled monolayers (SAMs) molecular technology, inverted PSCs employing SAMs as the hole transport layer (HTL) have achieved a power conversion efficiency (PCE) of 27.3% [4]. However, the poor wettability of the non-polar SAM surface toward the perovskite precursor solution disrupts perovskite crystal nucleation, leading to halide-deficient lattices and instability at the buried interface [5–7]. Consequently, the HTL/perovskite interface becomes highly susceptible to environmental stressors such as heat, moisture, and UV light, promoting chemical degradation of the perovskite and posing a major challenge to the stability of inverted PSCs [7–11].

To overcome this critical bottleneck, researchers have explored various strategies to improve the buried interfacial quality, such as improving wettability via hybrid SAMs [7, 12], introducing functional interlayers [13, 14], and designing multifunctional SAMs with high binding energy [15–17]. Among these, the utilization of interfacial modifiers with multifunctional groups has emerged as a promising avenue, where their strengthened interactions with the perovskite contribute to improved buried interface quality [18, 19]. The acidic-weakened boric acid functionalized molecular combines superior interfacial compatibility with multi-site coordination to perovskite precursors, facilitating the formation

of high-quality buried interfaces [20–22]. For example, Guo et al. [21]. introduced excess boric acid-functionalized molecules, which improved perovskite deposition and formed a coherent, well-passivated buried interface. Besides, electron-donating groups have been shown to modulate intramolecular electron density distribution, which promotes molecular polarization and reinforces its electrostatic interactions with perovskites [23–26]. However, the functional potential of these molecules critically depends on the spatial arrangement of their groups, requiring careful molecular design to ensure optimal performance. Liang et al. [24]. systematically compared the F substitution positions of F-PEAI and confirmed that *para*-F-PEAI (*p*-F-PEAI) possesses the most symmetric charge distribution and minimal steric hindrance, thereby exhibiting the strongest interfacial interactions with perovskite. It is important to note that achieving optimal functionality requires consideration of both the intrinsic properties of the functional group and its spatial position [27–29]. For instance, ortho-(phenylene)di(ethylammonium) iodide (*o*-$PDEAI_2$) enables the formation of a more stable surface 2D perovskite phase compared with meta (*m*)- and *p*- sites, boosting both the efficiency and operational stability of PSCs [30]. This structure-anchoring relationship is crucial at the buried interface, especially during the crystallization process of perovskites. Unstable anchoring compromises the effectiveness of interfacial passivation and may promote interface modifier desorption during crystallization, leading to a passivation failure that negates its intended function [23, 31]. This progress that 3,4,5-trifluorophenylboronic enables improved buried interface quality [32], has stimulated our curiosity about the underlying mechanisms and identifying the molecular configurations required for such interfacial regulation. Accordingly, designing multifunctional modifiers capable of forming cooperative and persistent binding at the perovskite surface is crucial for stabilizing buried interfaces and sustaining long-term device performance.

Herein, we systematically investigate the interaction between trifluorophenylboronic acid (TFBA) isomers and adjacent halogen vacancies in the perovskite octahedron to design 5-fluoro-6-hydroxypyridin-3-ylboronic acid (FO-PyBA) to stabilize the buried interface. By replacing the para-position F atom with a carbonyl (C = O) group and introducing a pyridinyl hydroxyl, FO-PyBA adopts a coplanar multidentate anchoring (CPMA) configuration on the perovskite surface, enabling cooperative C = O—Pb and B—O—Pb coordination along with N—H···I and O—H···I hydrogen bonding, thereby reinforcing the perovskite octahedral framework. Crucially, this more stable multidentate anchoring is enabled by precisely tailoring the interatomic distances of anchoring sites in derivatives to match the defect sites of perovskite. Molecular dynamics results indicate that the robust CPMA of FO-PyBA effectively inhibits octahedron distortion of perovskite and iodide migration. Therefore, the FO-PyBA effectively reduces interfacial nonradiative recombination and modulates the interfacial electronic structure. These effects enabled FO-PyBA-based PSCs to exhibit the best performance with an efficiency of 26.85% (certificated 26.70%, 0.08 cm^2) and 25.83% (1 cm^2), respectively. Remarkably, the PSCs retained 92% and 94% of their initial efficiencies after 1200 h aging in UV irradiation and 1000 h of operating under one-sun illumination in an N_2-filled glovebox, respectively, demonstrating excellent long-term stability.

2 | Results and Discussion

2.1 | Design of Interfacial Modifier Molecules

To optimize the buried interface, we employed arylboronic acid derivative interface modifiers, whose superior interfacial compatibility with multi-site coordination to perovskite precursors facilitates uniform precursor binding and the formation of high-quality buried interfaces [20–22]. Therefore, TFBA isomers bearing boronic acid (–$B(OH)_2$) and F substituents with different configurations were investigated, namely 2,4,6-trifluorophenylboronic acid (*m*-TFBA), 2,3,4-trifluorophenylboronic acid (*o*-TFBA), and 3,4,5-trifluorophenylboronic acid (*p*-TFBA) (Figure S1). First, we conducted a systematic investigation using DFT calculations on the bonding mechanisms between TFBA isomers and the perovskite surface. The results indicate that the TFBA isomers tend to adopt a parallel configuration orientation, forming two coordination bonds with the adjacent halogen vacancies in the perovskite octahedron, owing to its interatomic distances of anchoring sites (~6.48 Å) matching the size of adjacent halogen vacancies of α-$FAPbI_3$ (~6.36 Å) (Figure S2 and Note S1). In the parallel configuration of TFBA isomers, the rational functional group distribution and coplanar negative potential region of *p*-TFBA promote the interaction of para-fluorine atoms with surface Pb^{2+}, forming a bidentate F—Pb bonding, which maximizes the interface anchoring ability of multifunctional groups (−1.95 eV). In contrast, *m*-TFBA and *o*-TFBA exhibit weaker interactions, with binding energies of −1.79 and −1.87 eV, respectively (Figure 1b).

Therefore, we propose that maximizing the multifunctional groups anchoring ability of arylboronic acid derivative on the perovskite surface hinges on satisfying the following three criteria (Figure 1a): (a) Axisymmetric arrangement of electron-donating anchoring groups on a benzene ring; (b) Interatomic distances of anchoring sites are designed to match the adjacent halogen vacancies in α-$FAPbI_3$ (~6.36 Å); (c) The molecule features a coplanar negative electrostatic potential distribution. Guided by these principles, 5-fluoro-6-hydroxypyridin-3-ylboronic acid (FO-PyBA) was designed by replacing the para-position F atom with a carbonyl (C = O) group and introducing a pyridinyl hydroxyl (Figure S3 and Note S2). The ESP map of FO-PyBA displays a negative-potential distribution on the boronic acid and carbonyl oxygen atoms, while the pyridinyl hydroxyl exhibits more positive potential, collectively forming a coplanar and highly polarized electrostatic surface (Figure S3f). The FO-PyBA adopts a coplanar multidentate anchoring (CPMA) configuration on the perovskite surface through C = O—Pb and B—O—Pb coordination, N—H···I and O—H···I hydrogen bonding interactions, reinforcing the perovskite octahedral framework. DFT results show that FO-PyBA exhibits robust binding to the perovskite surface (−2.49 eV) than TFBA isomers (Figure 1b). The Crystal Orbital Hamilton Populations (COHP) [33] value effectively reflects the chemical bond strength of these derivatives on the perovskite surface (Figure 1c; Figure S4). The spatial para-position of F substituents in *p*-TFBA exhibits bidentate chelation with COHP values of −0.11 and −0.13 eV, respectively, which are significantly stronger than the monodentate chelation observed in other isomers. Notably, relative to TFBA isomers, the more stable C = O—Pb coordination

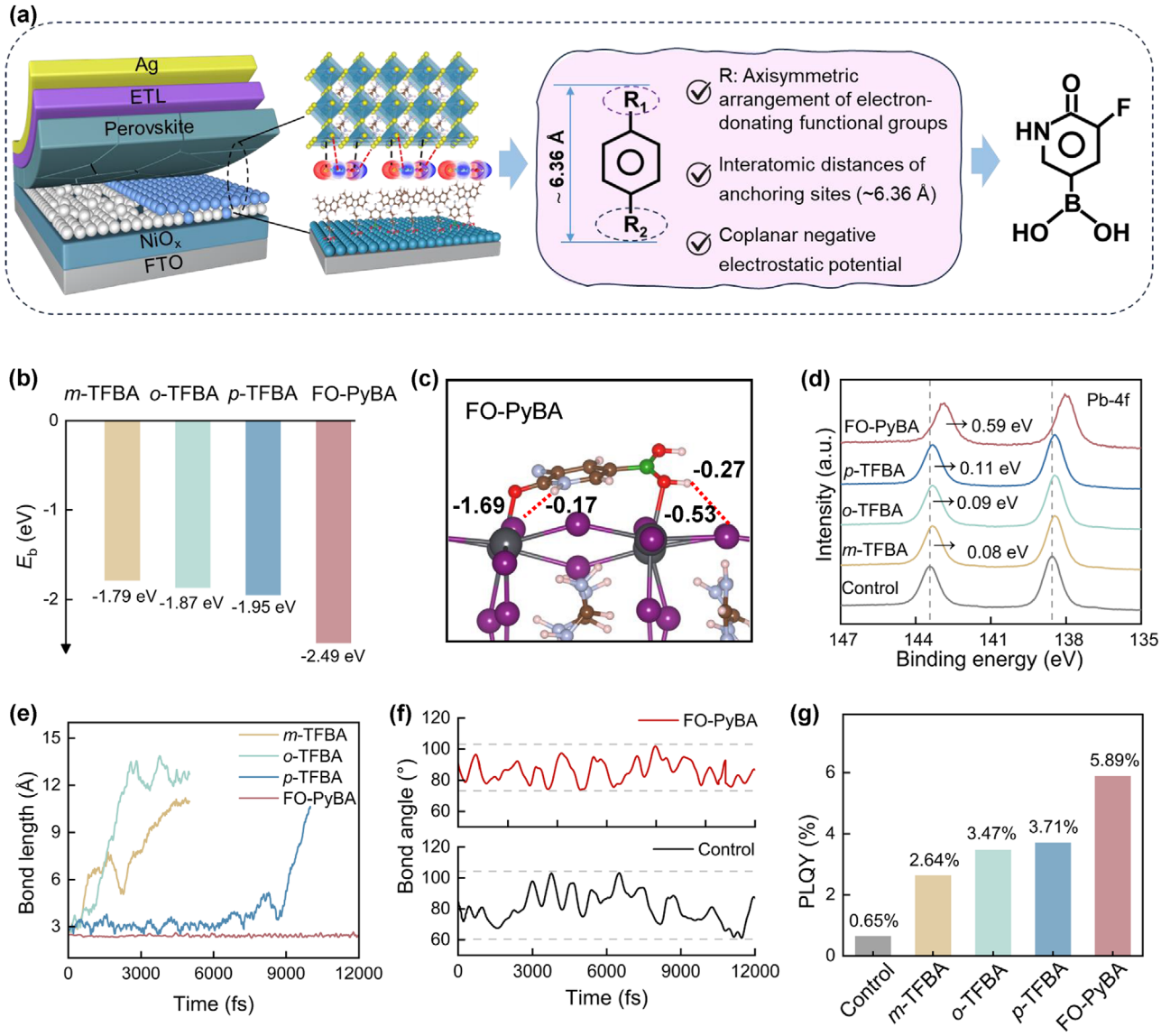

FIGURE 1 | Interaction and configuration between arylboronic acid derivatives and perovskite. (a) Schematic diagram of coplanar multidentate anchoring for buried interface. (b) The binding energies of parallel bonding configurations of arylboronic acid derivatives on the PbI-terminated $FAPbI_3$ (100) surface. (c) The FO-PyBA on the PbI-terminated $FAPbI_3$ (100) surface with the ICOHP value. (d) XPS spectra of Pb 4f. (e) Time-dependent evolution of B—O—Pb bond lengths for TFBA isomers and C = O—Pb bond lengths for FO-PyBA on the $FAPbI_3$ (100) surface. (f) Time-dependent bond angles of I—Pb—I in $FAPbI_3$ without and with FO-PyBA. (g) The PLQY of control, and arylboronic acid derivatives-treated HTLs based perovskite films.

(−1.69 eV) serves as the dominant contributor to maintaining the anchoring of the derivatives on the perovskite surface.

The X-ray photoelectron spectroscopy (XPS) was performed to further confirm the interaction between different interface modifiers and the perovskite. As shown in Figure 1d, the Pb $4f_{5/2}$ and Pb $4f_{7/2}$ peaks of the control film, located at 143.41 and 138.52 eV, respectively, shifted toward lower binding energies after these derivatives-treated. This shift indicates that derivatives donated electrons to the undercoordinated Pb^{2+}. Compared with TFBA isomers, the binding energy shift of FO-PyBA is 0.58 eV of the Pb $4f_{5/2}$ peaks toward lower binding energy, indicating the enhanced interaction between FO-PyBA and Pb^{2+}. Furthermore, these derivatives-based perovskite films display decreased I 3d binding energies compared with the control (Figure S5), implying that the halide ions also engage in hydrogen bonding with the derivatives, which can fix halide ions in the perovskite lattice to inhibit ion migration. The I 3d peaks of FO-PyBA shift by 0.59 eV relative to *p*-TFBA (0.23 eV). These pronounced peak shifts indicate that the FO-PyBA markedly enhanced anchoring strength on perovskite surface compared with the TFBA isomers.

To further investigate the structural stability of these derivatives anchoring configurations, we conducted ab initio molecular dynamics (AIMD) simulations. First, we monitored the temporal evolution of the strongest interfacial bond length between each derivative and the perovskite surface. The temporal evolution of interfacial bonding configurations reveals that FO-PyBA maintains robust C = O—Pb coordination (Figure 1e) during the simulation, which ensures a stable anchoring configuration and preserves the octahedral integrity of the perovskite lattice. In contrast, *p*-TFBA exhibits pronounced fluctuations in anchoring

distance and desorbs from the surface at around 8000 fs, indicative of an unstable interfacial structure and weaker coupling with surface Pb sites. Furthermore, *m*-TFBA and *o*-TFBA readily desorb from the perovskite surface at the initial stage of the simulation. This result indicates that the molecular configuration is critical for establishing a stable anchoring configuration. Subsequently, we monitor the time-dependent evolution of I—Pb—I bond angles within the perovskite lattice with and without FO-PyBA anchoring (Figure 1f). In the control-based perovskite, the bond angles fluctuate widely between 61° and 103°, indicating significant lattice distortion and the presence of non-radiative recombination centers that impair device efficiency and stability. In contrast, the FO-PyBA-based perovskite maintains a more stable I—Pb—I angle range of 74° to 102°. The corresponding standard deviation of the bond angle is significantly reduced in FO-PyBA-based perovskite (Figure S6), indicating effective suppression of perovskite lattice distortion and preservation of lattice integrity [34]. The root mean square displacement of the I^- ions, representing the inorganic Pb—I framework, in FO-PyBA-based perovskite surface remains the lowest compared with the control (Figure S7). The migration barrier of I^- ions increased from 0.346 to 0.902 eV (Figure S8), which indicates that FO-PyBA effectively inhibits iodide ion migration by forming robust CPMA with undercoordinated Pb^{2+} and I^- ions.

Ion absence of halide ions within perovskite lattices is the primary origin of non-radiative recombination. We further investigated the ability of arylboronic acid derivatives interfacial treatment to suppress defects at the buried interface of perovskites. As shown in Figure S9, the defect formation energy results confirm that the interface modifier can effectively suppress the formation of V_{Pb} and V_I on the perovskite surface, following the order: FO-PyBA > *p*-TFBA > *o*-TFBA > *m*-TFBA > control. This result indicates that the robust CPMA of FO-PyBA enables a more efficient suppression of defect formation, implying that it has fewer non-radiative recombination sites. We experimentally incorporated these derivatives as interface modifiers to fabricated the perovskite films, employing photoluminescence quantum yield (PLQY) measurements to quantify interface non-radiative recombination loss. Remarkably, the FO-PyBA-based perovskite film exhibits the highest PLQY (5.89%) among all these derivatives treated-HTLs-based films (Figure 1g).

To explore the interaction between the arylboronic acid derivatives and NiO_x, XPS spectra analysis was conducted. As shown in Figure S10a, the XPS spectra of NiO_x/Me-4PACz film exhibit Ni $2p_{3/2}$ peaks at 860.02 and 854.20 eV, corresponding to Ni^{3+} and Ni^{2+}, respectively. Upon treatment with arylboronic acid derivatives, Ni^{3+} peak positions shift toward lower binding energies by 0.12, 0.07, 0.12, and 0.09 eV, respectively. This shift was further evidenced by the increased Ni^{3+}/Ni^{2+} ratios, which from 1.21 reached 1.40, 1.44, 1.61, and 1.81, respectively. It reflects an improved surface chemical environment, which benefits the long-term stability of the buried interface. The O shifts to a higher energy level than NiO_x/Me-4PACz film (Figure S10b), indicating that the boronic acid in arylboronic acid derivatives interacts with NiO_x.

We then examined the impact of different derivatives treatment on charge transfer at the perovskite/HTL interface. As shown in Figure S11, the KPFM results show that the FO-PyBA-treated HTL displays a lower average surface potential compared to the control and TFBA isomers-treated. The hole conductivity and mobility were measured using devices with the structure FTO/NiO_x/Me-4PACz/(with or without arylboronic acid derivatives)/Ag, as shown in Figures S12 and S13. The derivative-treated HTLs exhibit markedly enhanced conductivity and hole mobility, enabling efficient hole transport and extraction while effectively suppressing charge accumulation at the HTL/perovskite interface, with the FO-PyBA–treated HTL delivering the most pronounced enhancement. We further calculated the density of states (DOS) to explore the effect of these derivatives on the electronic properties of the perovskite surface. As shown in Figure S14, the DOS near the conduction band minimum (CBM) and the valence band maximum (VBM) of the TFBA isomers and FO-PyBA-based perovskite surface have increased compared to the control. This indicates a redistribution of charge carriers and enhanced p-type conductivity at the perovskite film surface, which facilitates more efficient carrier transport [35, 36].

2.2 | Effect on Crystallization of Perovskite Films

To elucidate how arylboronic acid derivatives affect perovskite layer formation, we first measured the contact angles of perovskite precursor solutions on derivative-treated HTLs, as shown in Figure S15. The contact angle was decreased from 40.59° for the control sample to 33.94° for *m*-TFBA, 29.78° for *o*-TFBA, 27.36° for *p*-TFBA, and 22.41° for FO-PyBA, respectively. Notably, FO-PyBA exhibits the lowest contact angle, which can be attributed to the enhanced interfacial interactions between the perovskite precursor and the modified interface. This improved wettability promotes homogeneous precursor distribution and optimized nucleation density during spin-coating, thereby regulating perovskite crystallization and promoting high-quality film formation. Subsequently, we performed in situ photoluminescence (PL) to monitor the perovskite crystallization during the spin-coating and annealing stages. As shown in Figure 2a,c, all perovskite precursor films exhibit prominent PL emission upon antisolvent dropping at 40 s during spin-coating, indicating the onset of perovskite nucleation in the wet film. The FO-PyBA-based perovskite film exhibits the strongest PL intensity among the control and TFBA-based films, indicating that its improved wettability provides more effective nucleation sites and an effective stabilized perovskite octahedron structure, which promotes the formation of defect-suppressed higher-quality perovskite templates.

During the annealing stage, perovskite films on control and arylboronic acid derivatives-treated HTLs exhibit a characteristic crystallization-dissolution-recrystallization growth behavior, indicating that these derivatives do not alter the growth dynamics of perovskite films (Figure 2b). As shown in Figure 2d, the in situ annealing extracted PL results show that the FO-PyBA-based perovskite film reaches its maximum PL intensity at ~121 s, which is significantly later than the control film that peaks at ~90 s (Figure 2d). In comparison, the films on substrates treated with *m*-TFBA, *o*-TFBA, and *p*-TFBA exhibit intermediate peak times of ~98, ~104, and ~112 s, respectively. The results reveal that these derivatives effectively retard the crystallization of the perovskite films, which originates from the robust interaction between the interfacial modifier and the perovskite precursor. Especially, the potent coordination between FO-PyBA and the precursor

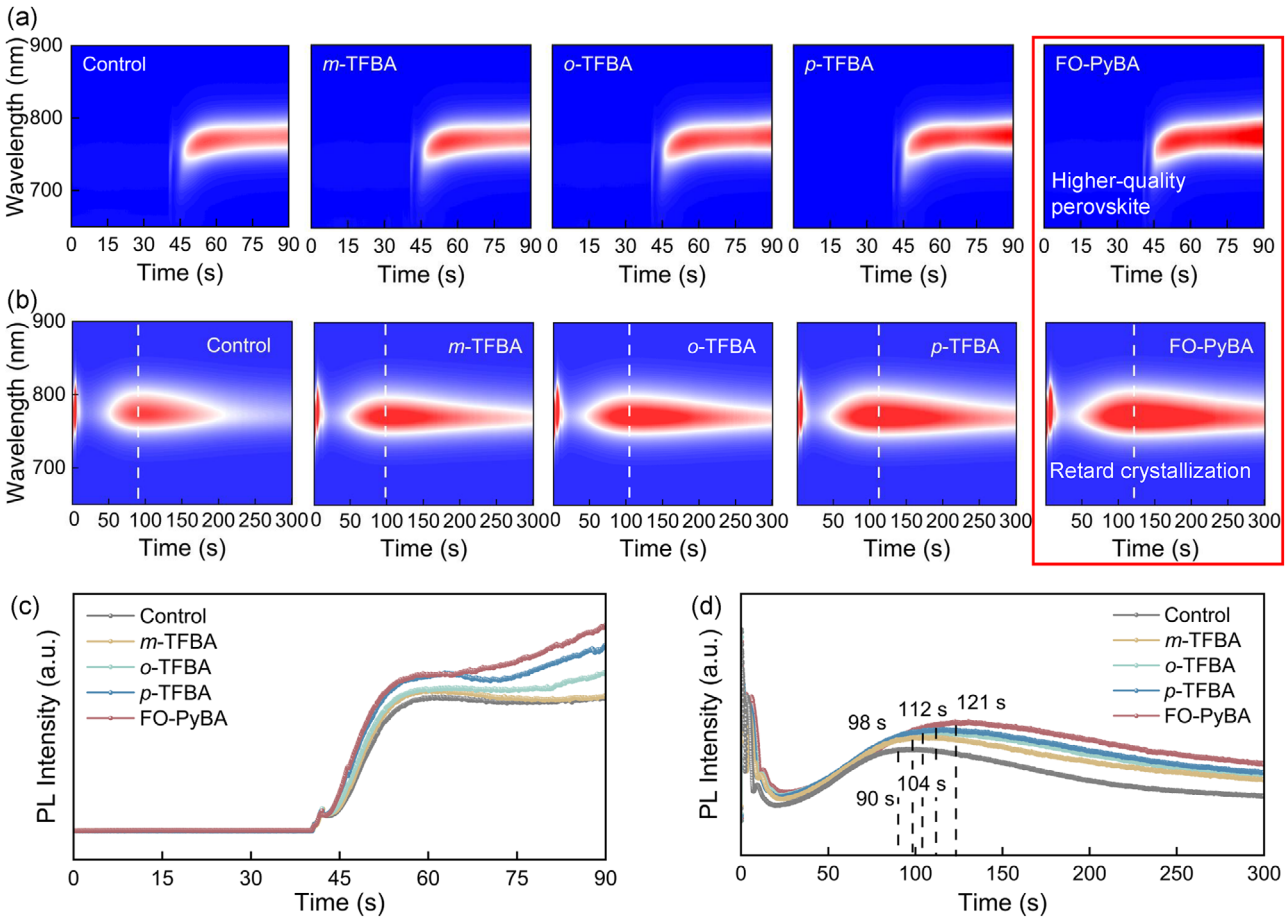

FIGURE 2 | In situ characterization of perovskite crystallization. (a) In situ PL spectra of control, arylboronic acid derivatives-treated HTLs based perovskite films during spin-coating and (b) annealing. The extracted PL curves from in situ PL during (c) spin-coating at 779 nm and (d) annealing at 775 nm of control and arylboronic acid derivatives-treated HTLs based perovskite films.

solution effectively modulates the crystallization kinetics, thereby governing the controlled crystal evolution. As the annealing proceeds, the PL intensity of all films gradually decreases due to lattice reorganization and the regeneration of non-radiative defect centers. However, the FO-PyBA-based film consistently maintains the highest PL intensity throughout the entire annealing stage owing to its robust CPMA.

2.3 | Photoelectric Properties of Perovskite Films

To evaluate the crystallization quality, scanning electron microscopy (SEM) images and grain size distribution of perovskite films deposited on different HTL substrates were obtained, as shown in Figure S16. The top-view SEM images reveal that all perovskite films exhibited uniform and dense morphologies without observable pinholes. Statistical analysis of the grain size distribution shows that the average grain diameter (D_{avg}) increases from 0.51 μm for the control film to 0.53 μm for *m*-TFBA, 0.54 μm for *o*-TFBA, 0.60 μm for *p*-TFBA, and 0.68 μm for FO-PyBA, respectively. This systematic increase in D_{avg} demonstrates that the introduction of arylboronic acid derivatives at the buried interface effectively promotes perovskite grain growth, with FO-PyBA delivering the most pronounced enhancement. Further cross-sectional SEM demonstrates that treatment with arylboronic acid derivatives effectively eliminates interfacial voids and cracks, thereby improving contact between the perovskite and the hole transport layer, while the FO-PyBA–based perovskite film simultaneously exhibits enlarged grains and highly ordered vertical grain growth (Figure S17).

The photoelectric properties of perovskite films were investigated through photoluminescence (PL) mapping, as shown in Figure 3a. The arylboronic acid derivatives-based perovskite films exhibited significantly enhanced PL intensity with bright yellow color within a 30 × 30 μm^2 confocal microscopy area. This indicates that these derivatives can suppress non-radiative recombination at the buried interface by bonding with under-coordinated Pb^{2+}/I^- sites. Specifically, among the derivatives interface-modified perovskite films, the FO-PyBA-based film exhibits the highest and most uniform PL intensity, attributed to its more homogeneous nucleation and the preservation of a stable and well-integrated perovskite octahedral framework. The steady-state PL and electroluminescence (EL) measurements are also shown in Figures S18 and S19. Both the PL and EL intensities sequentially decrease in the order of FO-PyBA > *p*-TFBA > *o*-TFBA > *m*-TFBA > control, indicating the improved film quality with fewer trap defects. Similar conclusions were drawn from the time-resolved photoluminescence (TRPL) spectra, as shown in Figure S20 and Table S1. The average carrier lifetime of the

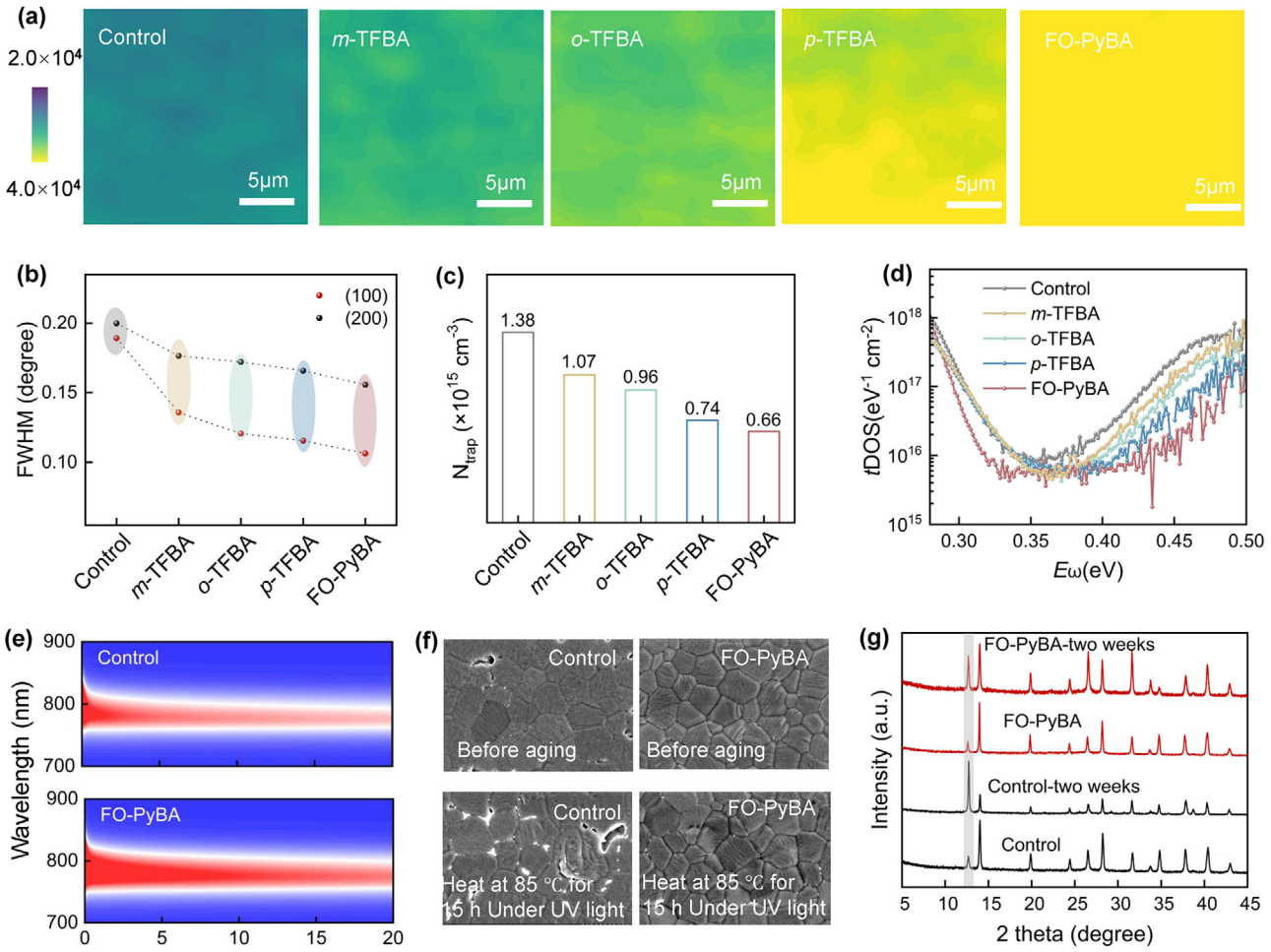

FIGURE 3 | Optoelectronic and stability characteristics of perovskite films. (a) PL mapping of control-, and arylboronic acid derivatives-based perovskite films. (b) FWHM of (100) and (200) peaks. (c) The defect density of control-, and arylboronic acid derivatives-based on perovskite films was measured by using SCLC measurement. (d) The *t*DOS analysis of control-, and arylboronic acid derivatives-based perovskite films. (e) In situ PL spectra of control- and FO-PyBA-based perovskite films at 85°C in N_2. (f) The bottom SEM of perovskite deposited on control and FO-PyBA-treated HTLs before and after aging at 85°C for 15 h under 254 nm UV lamp with an intensity of ~50 mW·cm^{-2} in an N_2 environment. (g) The XRD of the perovskite films deposited on control and FO-PyBA-treated HTL under 85°C in an air atmosphere (RH = 40%–50%).

control-based perovskite film is determined to be 333.28 ns. In contrast, the carrier lifetimes of the *m*-TFBA, *o*-TFBA, *p*-TFBA, and FO-PyBA-based perovskite films increased to 441.47, 447.77, 559.45, and 745.63 ns, respectively. These results demonstrate that the introduction of arylboronic acid derivatives at the buried interface of the perovskite film effectively suppresses defect-related non-radiative recombination. The optical absorption properties of perovskite films were also investigated, as shown in Figure S21. It was obvious that the FO-PyBA-based perovskite films show increased light absorption, which is beneficial for the light harvesting of PSCs.

In addition, X-ray diffraction (XRD) has been performed to further characterize the crystallinity of perovskite films. In Figure S22, two strong diffraction peaks observed at 14.14° and 28.28° belong to (100) and (200) crystal planes. The half maximum (FWHM) value was also calculated for the perovskite films, showing a decrease in the (100) planes FWHM value from 0.19° in the control-based perovskite film to 0.11° in the FO-PyBA-based perovskite film, whereas the (200) planes FWHM value decreases from 0.20° to 0.16°, confirming the increase in crystallinity (Figure 3b). Defect density analysis via space-charge-limited current (SCLC) measurements corroborates these results, as shown in Figure 3c and Figure S23. The calculated trap density is decreased from 1.38×10^{15} cm^{-3} for control-based perovskite film to 1.07×10^{15} cm^{-3} for *m*-TFBA, 0.96×10^{15} cm^{-3} for *o*-TFBA, 0.74×10^{15} cm^{-3} for *p*-TFBA, and 0.66×10^{15} cm^{-3} for FO-PyBA, respectively. Furthermore, the relationship between the defect density of states (*t*DOS) and energy level depth reveals that the deep-level defects at grain boundaries and buried surfaces are significantly reduced in FO-PyBA-based devices compared to the control- and TFBA-based (Figure 3d).

We next systematically evaluate the thermal, photoinduced, and moisture stability of the perovskite films. In particular, in situ PL monitoring of the perovskite films during thermal aging at 85°C in a N_2-filled glovebox is employed to capture the onset and progression of thermal quenching, providing direct insight into the intrinsic stability of the perovskite lattice. As the aging time increased, the PL intensity of the control-based perovskite films progressively decreased, whereas the FO-PyBA-treated film shows a relatively slow decay, with its intensity significantly

higher than that of the control (Figure 3e; Figure S24). These results indicate that the FO-PyBA effectively mitigates structural degradation, thereby enhancing the thermal stability of the perovskite films. To assess the stability of the buried interface before and after FO-PyBA treatment, we conducted an aging test under UV irradiation and thermal stress at 85°C on the perovskite films. As shown in Figure 3f, the perovskite film deposited on FO-PyBA-treated HTL exhibits a pronounced reduction in nanoscale voids at grain boundaries compared with the control HTL before aging, forming a highly uniform and compact film morphology. But during aging, the control films undergo severe morphological degradation, while the FO-PyBA-based perovskite films retain a uniform and compact morphology owing to the stability perovskite octahedral framework in the buried interface. In particular, the extensive PbI_2 aggregation observed at grain boundaries in the control film is almost completely suppressed in the FO-PyBA-based film.

Environmental stability of perovskite films was further evaluated by aging samples with and without FO-PyBA treatment under 40%–50% relative humidity (RH). As shown in Figure 3g, both films exhibited increased PbI_2 diffraction peaks after two weeks, indicative of perovskite decomposition. However, control-based perovskite films degraded faster than those based on FO-PyBA. These results highlight the effectiveness of FO-PyBA stabilized perovskite octahedra framework in mitigating moisture-induced degradation. The stabilization mechanism formed by FO-PyBA with CPMA on the perovskite surface slows down decomposition kinetics and enhances the durability of the film under the combined effects of thermal and humidity stress, providing critical insights into strategies for improving perovskite lattice stability.

2.4 | Photovoltaic Performance of PSCs

Inverted PSCs with the structure FTO/NiO_x/[4-(3,6-dimethyl-9H-carbazol-9-yl) butyl] phosphonic acid (Me-4PACz) /$FA_{0.9}Cs_{0.05}MA_{0.05}PbI_3$/PDADI/$C_{60}$/BCP/Ag were fabricated to assess device performance. We first optimized the concentrations of these derivatives, and the statistical photovoltaic performance along with the corresponding parameters is presented in Figures S25–S28 and Tables S2–S5. Each derivatives show optimal performance at a concentration of 0.2 mg·mL^{-1} (Figure S29). Accordingly, all subsequent TFBA- and FO-PyBA-treated HTLs were fabricated using this concentration. The statistical photovoltaic performance of 40 devices based on different HTLs with an active area of 0.08 cm^2 is shown in Figure 4a and Figures S30 and S31 and Table S6 exhibit an increasing trend in average PCE in the order of control < *m*-TFBA < *o*-TFBA < *p*-TFBA < FO-PyBA, accompanied by a significantly narrower distribution. The FWHM of the PCE distribution fitting curve was significantly decreased from 0.49 for the control to 0.40 for the FO-PyBA-based PSCs, reflecting the excellent fabrication reliability. This enhancement is mainly attributed to the notable improvements in open-circuit voltage (V_{OC}) and fill factor (FF), while the short-circuit current density (J_{SC}) remains nearly unchanged. The increased V_{OC} and FF are closely associated with the reduced interfacial nonradiative recombination and modulate the interfacial electronic structure to enhance charge extraction. The champion power conversion efficiency (PCE) of different HTLs-based PSCs is shown in Figure 4b and Table S7. The FO-PyBA-based PSCs achieved the highest PCE of 26.85% compared to TFBA-based PSCs, with a V_{OC} of 1.190 V, an FF of 86.50%, and a J_{SC} of 26.08 mA·cm^{-2}. One of the best-performing FO-PyBA-based PSCs has been sent to a third-party, achieving a certificated efficiency of 26.70% (Figure S32). In contrast, control-based PSC only achieved a PCE of 24.99%, with a V_{OC} of 1.174 V, an FF of 81.99%, and a J_{SC} of 25.97 mA·cm^{-2}. As shown in Figure S33, the integrated J_{SC} obtained from the external quantum efficiency (EQE) of the control and champion FO-PyBA-based PSCs are 25.5 and 25.8 mA·cm^{-2}, respectively, which is consistent with the J_{SC} values from the *J*–*V* curves. The hysteresis index (HI) was also calculated for the control and FO-PyBA-based PSCs, showing a decrease from 0.019 (control) to 0.002 (FO-PyBA), confirming the suppression of interfacial defects and ionic migration (Figure S34 and Table S8). In addition, the stabilized power output of both PSCs was measured under maximum power point tracking (Figure S35). The FO-PyBA-based PSC achieved a PCE of 26.01% with negligible decay over 300 s, whereas the control-based PSC exhibited a decline from 24.26% to 23.35%.

To evaluate the potential of FO-PyBA for large-area industrial applications, PSCs with an active area of 1 cm^2 were prepared (Figure 4c; Table S9). The champion FO-PyBA-based PSC delivered a PCE of 25.83%, outperforming the control counterpart (23.90%), demonstrating the exceptional capability of FO-PyBA to enable high-quality and large-area perovskite films. In addition, we prepared a wide bandgap perovskite (1.67 eV) on FO-PyBA-treated HTL to assess its universality. As shown in Figure 4d, the champion FO-PyBA-based PSCs achieved a PCE of 23.44% (J_{SC} = 22.30 mA·cm^{-2}, V_{OC} = 1.243 V, FF = 84.55%), outperforming the control-based PSCs with a PCE of 21.86% (J_{SC} = 21.99 mA·cm^{-2}, V_{OC} = 1.209 V, FF = 82.23%). The PCE distribution histogram (Figure 4e; Table S10) further confirms the performance advantage, with the FO-PyBA-based PSC exhibiting an average PCE of 23.07% versus 21.46% for the control. These results highlight the universal applicability of the FO-PyBA to effectively suppress defect generation in enhancing photovoltaic performance across different perovskite bandgaps, supporting its potential for the commercialization of tandem PSCs.

Electrochemical impedance spectroscopy (EIS), dark *J*–*V* characterization, and ideality factor (n_{ID}) analysis were employed to explore the underlying device physics. EIS analysis revealed that the recombination resistance (R_{rec}) increased from 2.18×10^5 to 3.46×10^5 Ω, while the series resistance (R_s) decreased from 21.91 to 19.43 Ω for control and FO-PyBA-based PSCs, respectively. These results indicate suppressed charge recombination and enhanced charge transport at the buried interface (Figure S36 and Table S11). To further investigate the dominant recombination mechanism, we examined the relationship between V_{OC} and light intensity using the equation:

$$V_{OC} = \frac{n_{ID} k_B T}{q} \ln(I)$$

where k_B is the Boltzmann constant, and q is the elementary charge. The extracted n_{ID} was 1.63 for control-based PSC and 1.39 for FO-PyBA-based PSC (Figure 4f), indicating that FO-PyBA effectively inhibited non-radiative recombination induced by intrinsic defects of perovskite [37]. This conclusion is further supported by the lower current leakage observed in the dark *J*–*V*

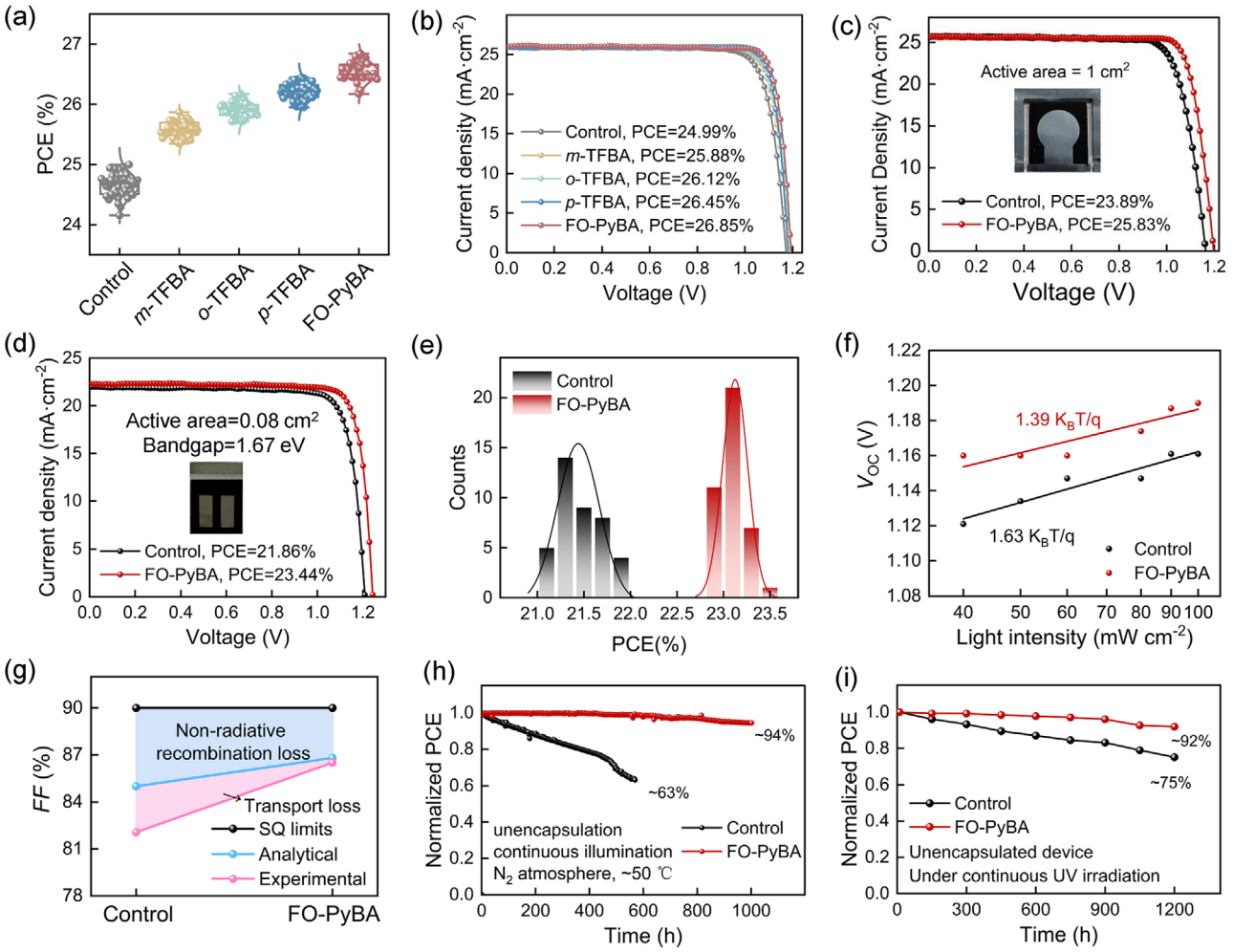

FIGURE 4 | Device performance. (a) Statistical photovoltaic parameter distributions of PCE for 40 devices (without and with) arylboronic acid derivatives treatment. (b) *J–V* curves (reverse scan) of the champion planar PSCs (without and with) arylboronic acid derivatives treatment; the area of the cell is 0.08 cm^2. (c) The *J–V* curves (reverse scan) of control and FO-PyBA-based PSCs with an active area of 1 cm^2. (d) The *J–V* curves (reverse scan) of control and FO-PyBA-based 1.67 eV wide-bandgap PSCs with an active area of 0.08 cm^2. (e) Distribution histograms of PCE value among 40 control and FO-PyBA-based 1.67 eV bandgap PSCs, respectively. (f) V_{OC} of PSCs with control-based and FO-PyBA-treated HTLs plotted against the logarithm of light intensity. (g) Plots of the SQ-limit FF, analytical FF, and the experimental FF for PSCs with control-based and FO-PyBA-treated HTLs. (h) The normalized SPO of the unencapsulated inverted PSCs under continuous one-sun illumination in N_2 glovebox. (i) PCE evolution of unencapsulated control and FO-PyBA-based PSCs stored under a 254 nm UV lamp with an intensity of ~50 $mW \cdot cm^{-2}$ in an N_2 environment.

curves (Figure S37). Subsequently, we compared the maximum FF with the experimental values to reveal the reasons for the enhancement of FF (Figure 4g). These results indicate that FO-PyBA-based PSCs exhibit lower non-radiative recombination and diminished charge transport losses than control-based PSCs. Collectively, these findings confirm that FO-PyBA effectively suppresses perovskite defects, mitigates carrier recombination, and facilitates more efficient interfacial charge transport, thereby enabling high-performance PSCs.

We further assessed the device stability of the unencapsulated device under diverse conditions. The FO-PyBA-based PSCs exhibited excellent operational stability under continuous white LED illumination (100 $mW \cdot cm^{-2}$) in N_2 atmosphere, retaining 94% of their initial PCE after 1000 h (Figure 4h). For UV stability evaluation, devices were irradiated under a 254 nm UV lamp in an N_2 environment. After 1200 h, the FO-PyBA-based PSC maintained 92% of its initial PCE, compared to 75% for the control-based PSCs (Figure 4i). Thermal stability tests conducted at 85°C in a N_2 atmosphere demonstrated that FO-PyBA-based PSCs retained 90% of their initial efficiency after 600 h (Figure S38). The enhanced device stability is attributed to the robust CPMA of FO-PyBA, which improves buried interfacial quality, thereby mitigating degradation pathways [31].

3 | Conclusion

In summary, FO-PyBA stabilizes the perovskite octahedral structure via the concurrent formation of C = O—Pb and B—O—Pb coordination bonds along with N—H···I and O—H···I hydrogen bonds to enhance the robustness of the buried interface. The robust CPMA of FO-PyBA constructs a high-quality buried interface, enabling efficiency and stable inverted PSCs. The FO-PyBA-based PSCs achieved a champion efficiency of 26.85% (certificated 26.7%) and 25.83% for active areas of 0.08 and 1

cm^2, respectively. The 1.67 eV wide-bandgap device attained an efficiency of 23.44%. More importantly, the unencapsulated device demonstrated excellent long-term stability, retaining 92% and 94% of its initial efficiency after 1200 h of aging under UV irradiation and 1000 h of operating under one-sun illumination, respectively. The robust anchoring of arylboronic acid derivatives on the perovskite surface reveals the critical importance of functional group design, spatial configuration, and steric effects in buried-interface engineering, while also establishing that only robust anchoring can effectively stable octahedral framework. The proposed robust CPMA provide a viable pathway to overcome buried interfacial instability and offers valuable insights into the development of high-performance and durable PSCs.

4 | Experimental Section

4.1 | Materials

Materials required for preparing the hole transport layer: Nickel oxide (NiO_x) and [4-(3,6-dimethyl-9*H*-carbazol-9-yl) butyl] phosphonic acid (Me-4PACz) were purchased from Vizuchem Co., Ltd (Shanghai, China). Materials required for fabricating the perovskite layer: cesium iodide (CsI, 99.98%), formamidinium iodide (FAI), methylammonium iodide (MAI, 99.9%), methylammonium chloride (MACl, 99.9%), lead(II) chloride($PbCl_2$, 99.9%), 1,3-Diaminopropane dihydroiodide (PDADI), 5-fluoro-6-hydroxypyridin-3-ylboronic acid (FO-PyBA) were purchased from Xi'an Yuri Solar Co., Ltd. Lead iodide (purity: 99.999%) was purchased from Tokyo Chemical Industry (TCI). Materials required for fabricating the electron transport layer: fullerene (C_{60}), 2,9-dimethyl-4,7-diphenyl-1,10-Phenanthroline (BCP) were purchased from Xi'an Yuri Solar Co.

4.2 | Device Fabrication

The F-doped tin oxide (FTO) glass (7 $\Omega \cdot sq^{-1}$) was sequentially ultrasonically cleaned with detergent (2 vol%), deionized (DI) water, ethanol, and DI water for 15 min, respectively. The FTO substrate was treated with ultraviolet ozone (UV-O) for 30 min. Then the substrate was spin-coated with a thin layer of NiO_x nanoparticle film (5 $mg \cdot mL^{-1}$ NiO_x water solution) at 3000 rpm for 30 s and annealed in ambient air at 150°C for 10 min. 0.5 $mg \cdot mL^{-1}$ Me-4PACz was deposited on the NiO_x at 4000 rpm for 30 s in a N_2 glovebox. Subsequently, 0.2 $mg \cdot mL^{-1}$ Trifluorophenylboronic acid isomers (IPA solution) was deposited on the hole transport layer at 4000 rpm for 30 s and annealed at 100°C for 5 min. 50 µL perovskite solutions were spin-coated onto HTL at 1000 rpm for 10 s, subsequently at 5000 rpm for 40 s. 200 µL CB was dripped onto the center of the film at 10 s before the end of spin-coating. The deposited perovskite films were subsequently annealed on a hotplate at 100°C for 30 min. 1$mg \cdot mL^{-1}$ PDADI was deposited on the perovskite at 4000 rpm for 30 s and annealed at 100°C for 5 min. For the electron transport layer (ETL), 20 nm C_{60} was thermally evaporated on the perovskite films at a rate of 0.2 $A \cdot s^{-1}$ under a high vacuum of ~10^{-7} Torr, followed by 7 nm BCP evaporation as a hole-blocking layer. Finally, a 100 nm Ag electrode was evaporated by thermal evaporation.

4.3 | Density Function Theory Calculations

All calculations were performed using the Vienna ab initio simulation package (VASP 5.4.4) [38, 39], and the exchange–correlation energy has been treated using the Perdew–Burke-Ernzerhof (PBE) function [40]. For the surface calculations, we constructed a 2 × 2 × 1 supercell system of PbI-terminated of α-$FAPbI_3$ (100) surface with a vacuum layer of more than 20 Å. The Brillouin zone integration was sampled with a 3 × 3 × 1 Γ-centered k-point grid with a plane wave energy cutoff of 500 eV. To explore the bonding mechanism of chemical bonds in the system, the Crystal Orbital Hamilton Population (COHP) method [41, 42] is used, which is calculated by using the Local Orbital Basis Suite toward Electronic-Structure Reconstruction (LOBSTER) software package [43, 44]. Ab initio molecular dynamics calculations were performed with the canonical ensemble condition (NVT) ensemble. The climbing-image nudged elastic band (CI-NEB) [45–47] and an improved dimer method (IDM) [48] were used to calculate the iodide migration energy barriers. The electrostatic potentials of the TFBA isomers were calculated using the Gaussian 09 package [49] at the B3LYP/def2-SVP [50–52] level with DFT-D3.

4.4 | Device Characterization

The surface and cross morphologies of perovskite films were measured using cold field-emission scanning electron microscopy (SEM, Hitachi S-4800). The XRD patterns of the perovskite films deposited on HTL were obtained on an X-ray diffractometer (D8 Advance, Bruker). PL mapping was carried out using a laser confocal fluorescence lifetime imaging microscope (Nikon-ARsiMP-LSM-Kit-Legend Elite-USX) with a 405 nm excitation wavelength. The current–voltage (*J–V*) characteristics of PSCs were measured using a Keithley 2400 Source Meter with a power density of 100 $mW \cdot cm^{-2}$. The external quantum efficiency (EQE) spectra of PSCs were achieved using a QE-R system (Enli Tech.).

Acknowledgements

This work is supported partially by the Key Research and Development Program sponsored by the Ministry of Science and Technology (MOST) (Grant no. 2022YFB4200301), Beijing Natural Science Foundation (Z240024), National Natural Science Foundation of China (Grant nos. 22109002, 22409061, 52302250, 52232008, 52102245, 52072121, 52402254, and 22409061), Beijing Nova Program (20220484016), Young Elite Scientists Sponsorship Program by CAST (2022QNRC001), 2022 Strategic Research Key Project of Science and Technology Commission of the Ministry of Education, Huaneng Group Headquarters Science and Technology Project (HNKJ20-H88), the Fundamental Research Funds for the Central Universities (2024MS038 and 2024JC005) and the NCEPU "Double First-Class" Program.

Conflicts of Interest

The authors declare no conflicts of interest.

Data Availability Statement

The data that support the findings of this study are available from the corresponding author upon reasonable request.

References

1. Q. Jiang and K. Zhu, "Rapid Advances Enabling High-Performance Inverted Perovskite Solar Cells," *Nature Reviews Materials* 9, no. 6 (2024): 399–419, https://doi.org/10.1038/s41578-024-00678-x.

2. S. Liu, V. P. Biju, Y. Qi, W. Chen, and Z. Liu, "Recent Progress in the Development of High-Efficiency Inverted Perovskite Solar Cells," *NPG Asia Materials* 15, no. 1 (2023): 27, https://doi.org/10.1038/s41427-023-00474-z.

3. Y. Yang, C. Liu, Y. Ding, et al., "A Thermotropic Liquid Crystal Enables Efficient and Stable Perovskite Solar Modules," *Nature Energy* 9, no. 3 (2024): 316–323, https://doi.org/10.1038/s41560-023-01444-z.

4. M. A. Green, E. D. Dunlop, M. Yoshita, et al., "Solar Cell Efficiency Tables (Version 66)," *Progress in Photovoltaics: Research and Applications* 33, no. 7 (2025): 795–810, https://doi.org/10.1002/pip.3919.

5. H. Tang, Z. Shen, Y. Shen, et al., "Reinforcing Self-Assembly of Hole Transport Molecules for Stable Inverted Perovskite Solar Cells," *Science* 383, no. 6688 (2024): 1236–1240, https://doi.org/10.1126/science.adj9602.

6. K. Hossain, A. Kulkarni, U. Bothra, et al., "Resolving the Hydrophobicity of the Me-4PACz Hole Transport Layer for Inverted Perovskite Solar Cells with Efficiency>20%," *ACS Energy Letters* 8, no. 9 (2023): 3860–3867, https://doi.org/10.48550/arXiv.2304.13788.

7. J. Chen, X. Wang, T. Wang, et al., "Determining the Bonding–Degradation Trade-Off at Heterointerfaces for Increased Efficiency and Stability of Perovskite Solar Cells," *Nature Energy* 10, no. 2 (2025): 181–190, https://doi.org/10.1038/s41560-024-01680-x.

8. M. De Bastiani, G. Armaroli, R. Jalmood, et al., "Mechanical Reliability of Fullerene/Tin Oxide Interfaces in Monolithic Perovskite/Silicon Tandem Cells," *ACS Energy Letters* 7 (2022): 827–833, https://doi.org/10.1021/acsenergylett.1c02148.s001.

9. J. Zhao, Y. Deng, H. Wei, et al., "Strained Hybrid Perovskite Thin Films and Their Impact on the Intrinsic Stability of Perovskite Solar Cells," *Science Advances* 3, no. 11 (2017): aao5616, https://doi.org/10.1126/sciadv.aao5616.

10. Z. Dai, S. K. Yadavalli, M. Chen, A. Abbaspourtamijani, Y. Qi, and N. P. Padture, "Interfacial Toughening with Self-Assembled Monolayers Enhances Perovskite Solar Cell Reliability," *Science* 372, no. 6542 (2021): 618–622, https://doi.org/10.1126/science.abf5602.

11. Z. Li, X. Sun, X. Zheng, et al., "Stabilized Hole-Selective Layer for High-Performance Inverted p-i-n Perovskite Solar Cells," *Science* 382, no. 6668 (2023): 284–289, https://doi.org/10.1126/science.ade9637.

12. S. Liu, J. Li, W. Xiao, et al., "Buried Interface Molecular Hybrid for Inverted Perovskite Solar Cells," *Nature* 632, no. 8025 (2024): 536–542, https://doi.org/10.1038/s41586-024-07723-3.

13. X. He, H. Chen, J. Yang, et al., "Enhancing Hole Transport Uniformity for Efficient Inverted Perovskite Solar Cells Through Optimizing Buried Interface Contacts and Suppressing Interface Recombination," *Angewandte Chemie* 136, no. 52 (2024): 202412601, https://doi.org/10.1002/ange.202412601.

14. J. Cao, W. Chen, C. Zhao, et al., "Realizing Mechanical Stable and Efficient Wide-Bandgap Flexible Perovskite Solar Cells by Toughening the Buried Interface," *Science China Materials* 68, no. 5 (2025): 1415–1423, https://doi.org/10.1007/s40843-024-3209-x.

15. J. Wang, B. Jiao, R. Tian, et al., "Less-Acidic Boric Acid-Functionalized Self-Assembled Monolayer for Mitigating NiOx Corrosion for Efficient All-Perovskite Tandem Solar Cells," *Nature Communications* 16, no. 1 (2025): 4148, https://doi.org/10.1038/s41467-025-59515-6.

16. G. Qu, L. Zhang, Y. Qiao, et al., "Self-Assembled Materials with an Ordered Hydrophilic Bilayer for High Performance Inverted Perovskite Solar Cells," *Nature Communications* 16, no. 1 (2025): 86, https://doi.org/10.1038/s41467-024-55523-0.

17. R. Zhao, Y. Du, N. Wu, et al., "Design of Multifunctional Phosphonic Acid Molecule for Highly Efficient, Stable Inverted Perovskite Solar Cells," *Science China Materials* (2025): 1–11, https://doi.org/10.1007/s40843-025-3643-8.

18. Y. Zhao, X. Luan, L. Han, and Y. Wang, "Post-Assembled Alkylphosphonic Acids for Efficient and Stable Inverted Perovskite Solar Cells," *Advanced Functional Materials* 34, no. 46 (2024): 2405646, https://doi.org/10.1002/adfm.202405646.

19. B. Yu, K. Wang, Y. Sun, and H. Yu, "Minimizing Buried Interface Energy Losses with Post-Assembled Chelating Molecular Bridges for High-Performance and Stable Inverted Perovskite Solar Cells," *Advanced Materials* 37, no. 14 (2025): 2500708, https://doi.org/10.1002/adma.202500708.

20. M. Abbas, B. Cai, J. Hu, F. Guo, Y. Mai, and X.-C. Yuan, "Improving the Photovoltage of Blade-Coated MAPbI3 Perovskite Solar Cells via Surface and Grain Boundary Passivation With π-Conjugated Phenyl Boronic Acids," *ACS Applied Materials & Interfaces* 13, no. 39 (2021): 46566–46576, https://doi.org/10.1021/acsami.1c11335.

21. H. Guo, C. Liu, H. Hu, et al., "Neglected Acidity Pitfall: Boric Acid-Anchoring Hole-Selective Contact for Perovskite Solar Cells," *National Science Review* 10, no. 5 (2023): nwad057, https://doi.org/10.1093/nsr/nwad057.

22. G. Zhang, C. Jin, Y. Gao, et al., "Postassembly Multifunctional Boric Acid Molecular-Modulated Buried Interface for High-Performance Inverted Perovskite Solar Cells," *ACS Sustainable Chemistry & Engineering* 13 (2025): 19297–19307, https://doi.org/10.1021/acssuschemeng.5c08637.

23. R. Lin, J. Xu, M. Wei, et al., "All-Perovskite Tandem Solar Cells with Improved Grain Surface Passivation," *Nature* 603, no. 7899 (2022): 73–78, https://doi.org/10.1038/s41586-021-04372-8.

24. X. Liang, X. Zhou, F. Wang, et al., "Judicious Fluorination of Perovskite Quantum Wells Enables over 25% Efficiency in Inverted Solar Cells," *Advanced Energy Materials* 14, no. 42 (2024): 2402243, https://doi.org/10.1002/aenm.202402243.

25. T. Wu, R. Zhao, J. Qiu, S. Wang, X. Zhang, and Y. Hua, "Enhancing the Hot Carrier Injection of Perovskite Solar Cells by Incorporating a Molecular Dipole Interlayer," *Advanced Functional Materials* 32, no. 38 (2022): 2204450, https://doi.org/10.1002/adfm.202204450.

26. J. Shi, M. W. Samad, F. Li, et al., "Dual-Site Molecular Dipole Enables Tunable Interfacial Field Toward Efficient and Stable Perovskite Solar Cells," *Advanced Materials* 36, no. 44 (2024): 2410464, https://doi.org/10.1002/adma.202410464.

27. X. Jiang, L. Zhu, B. Zhang, et al., "Spatial Conformation Engineering of Aromatic Ketones for Highly Efficient and Stable Perovskite Solar Cells," *Journal of the American Chemical Society* 146, no. 50 (2024): 34833–34841, https://doi.org/10.1021/jacs.4c13866.

28. X. Jiang, S. Qin, L. Meng, et al., "Isomeric Diammonium Passivation for Perovskite–Organic Tandem Solar Cells," *Nature* 635, no. 8040 (2024): 860–866, https://doi.org/10.1038/s41586-024-08160-y.

29. X. Zhao, J. Zhou, S. Wang, et al., "Effects of N-Positions on Pyridine Carboxylic Acid-Modified Inverted Perovskite Solar Cells," *ACS Applied Energy Materials* 4, no. 7 (2021): 6903–6911, https://doi.org/10.1021/acsaem.1c01017.

30. C. Liu, Y. Yang, K. Rakstys, et al., "Tuning Structural Isomers of Phenylenediammonium to Afford Efficient and Stable Perovskite Solar Cells and Modules," *Nature Communications* 12, no. 1 (2021): 6394, https://doi.org/10.1038/s41467-021-26754-2.

31. F. Pei, S. Lin, Z. Zhang, et al., "Inhibiting Defect Passivation Failure in Perovskite for Perovskite/Cu(In, Ga)Se2 Monolithic Tandem Solar Cells with Certified Efficiency 27," *Nature Energy* 10 (2025): 1–12, https://doi.org/10.1038/s41560-025-01761-5.

32. J. Yang, Z. Zhao, C. Ding, et al., "Buried Interface Passivation With 3, 4, 5-Trifluorophenylboronic Acid Enables Efficient and Stable Inverted Perovskite Solar Cells," *ACS Applied Materials & Interfaces* 17, no. 11 (2025): 16844–16854, https://doi.org/10.1021/acsami.4c21627.

33. R. Nelson, C. Ertural, J. George, V. L. Deringer, G. Hautier, and R. Dronskowski, "LOBSTER: Local Orbital Projections, Atomic Charges, and Chemical-Bonding Analysis From Projector-Augmented-Wave-Based Density-Functional Theory," *Journal of Computational Chemistry* 41, no. 21 (2020): 1931–1940, https://doi.org/10.1002/jcc.26353.

34. L. Kong, Y. Sun, B. Zhao, et al., "Fabrication of Red-Emitting Perovskite Leds by Stabilizing Their Octahedral Structure," *Nature* 631, no. 8019 (2024): 73–79, https://doi.org/10.1038/s41586-024-07531-9.

35. W. Xiong, W. Tang, G. Zhang, et al., "Controllable P-and N-Type Behaviours in Emissive Perovskite Semiconductors," *Nature* 633, no. 8029 (2024): 344–350, https://doi.org/10.1038/s41586-024-07792-4.

36. W. Yang, Y. Lin, W. Zhu, et al., "Charge Polarization Tunable Interfaces for Perovskite Solar Cells and Modules," *Advanced Materials* 37 (2025): 2502865, https://doi.org/10.1002/adma.202502865.

37. L. Yang, J. Feng, Z. Liu, et al., "Record-Efficiency Flexible Perovskite Solar Cells Enabled by Multifunctional Organic Ions Interface Passivation," *Advanced Materials* 34, no. 24 (2022): 2201681, https://doi.org/10.1002/adma.202201681.

38. G. Kresse and D. Joubert, "From Ultrasoft Pseudopotentials to the Projector Augmented-Wave Method," *Physical Review B* 59, no. 3 (1999): 1758–1775, https://doi.org/10.1103/PhysRevB.59.1758.

39. G. Kresse and J. Furthmuller, "Efficient Iterative Schemes for Ab Initio Total-Energy Calculations Using a Plane-Wave Basis Set," *Physical Review B* 54, no. 16 (1996): 11169–11186, https://doi.org/10.1103/PhysRevB.54.11169.

40. J. Perdew, K. Burke, and M. Ernzerhof, "Generalized Gradient Approximation Made Simple," *Physical Review Letters* 77, no. 18 (1996): 3865–3868, https://doi.org/10.1103/PhysRevLett.77.3865.

41. V. Deringer, A. Tchougreeff, and R. Dronskowski, "Crystal Orbital Hamilton Population (COHP) Analysis as Projected From Plane-Wave Basis Sets," *Journal of Physical Chemistry* 115, no. 21 (2011): 5461–5466, https://doi.org/10.1021/jp202489s.

42. R. Dronskowski and P. Bloechl, "Crystal Orbital Hamilton Populations (COHP): Energy-Resolved Visualization of Chemical Bonding in Solids Based on Density-Functional Calculations," *The Journal of Physical Chemistry* 97, no. 33 (1993): 8617–8624, https://doi.org/10.1021/j100135a014.

43. S. Maintz, V. L. Deringer, A. L. Tchougréeff, and R. Dronskowski, "LOBSTER: A Tool to Extract Chemical Bonding From Plane-Wave Based DFT," *Journal of Computational Chemistry* 37, no. 11 (2016): 1030–1035, https://doi.org/10.1002/jcc.24300.

44. S. Maintz, V. L. Deringer, A. L. Tchougréeff, and R. Dronskowski, "Analytic Projection From Plane-Wave and PAW Wavefunctions and Application to Chemical-Bonding Analysis in Solids," *Journal of Computational Chemistry* 34, no. 29 (2013): 2557–2567, https://doi.org/10.1002/jcc.23424.

45. G. Mills, H. Jonsson, and G. Schenter, "Reversible Work Transition State Theory: Application to Dissociative Adsorption of Hydrogen," *Surface Science* 324, no. 2–3 (1995): 305–337, https://doi.org/10.1016/0039-6028(94)00731-4.

46. G. Henkelman and H. Jónsson, "Improved Tangent Estimate in the Nudged Elastic Band Method for Finding Minimum Energy Paths and Saddle Points," *The Journal of Chemical Physics* 113, no. 22 (2000): 9978–9985, https://doi.org/10.1063/1.1323224.

47. G. Henkelman, B. Uberuaga, and H. Jónsson, "A Climbing Image Nudged Elastic Band Method for Finding Saddle Points and Minimum Energy Paths," *The Journal of Chemical Physics* 113, no. 22 (2000): 9901–9904, https://doi.org/10.1063/1.1329672.

48. A. Heyden, A. Bell, and F. Keil, "Efficient Methods for Finding Transition States in Chemical Reactions: Comparison of Improved Dimer Method and Partitioned Rational Function Optimization Method," *The Journal of Chemical Physics* 123, no. 22 (2005): 7010, https://doi.org/10.1063/1.2104507.

49. M. J. Frisch, G. Trucks, H. B. Schlegel, et al., *Gaussian 09 Revision E01* (Gaussian, Inc., 2013).

50. A. Becke, "Density-Functional Thermochemistry. III. The Role of Exact Exchange," *The Journal of Chemical Physics* 98 (1993): 5648–5652, https://doi.org/10.1063/1.464913.

51. P. J. Stephens, F. J. Devlin, C. F. Chabalowski, and M. J. Frisch, "Ab Initio Calculation of Vibrational Absorption and Circular Dichroism Spectra Using Density Functional Force Fields," *The Journal of Physical Chemistry* 98 (1994): 11623–11627, https://doi.org/10.1021/j100096a001.

52. P. Chen, M. Gu, X. Huang, M. Wang, Y. Lin, and G. Chen, "DFT Study on the C–NO Coupling Reaction With Different Active Sites," *Combustion Science and Technology* 193 (2021): 541–560, https://doi.org/10.1080/00102202.2019.1663415.

Supporting Information

Additional supporting information can be found online in the Supporting Information section.

Supporting File: adma72592-sup-0001-SuppMat.docx.